Atomically Dispersed Fe-N$_4$ Modified with Precisely Located S for Highly Efficient Oxygen Reduction

Yin Jia[1], Xuya Xiong[4], Danni Wang[2], Xinxuan Duan[1], Kai Sun[1,3], Yajie Li[1], Lirong Zheng[5], Wenfeng Lin[3], Mingdong Dong[4], Guoxin Zhang[2] ✉, Wen Liu[1] ✉, Xiaoming Sun[1] ✉

Yin Jia and Xuya Xiong have contributed equally to this work.

✉ Guoxin Zhang, zhanggx@sdust.edu.cn; Wen Liu, wenliu@mail.buct.edu.cn; Xiaoming Sun, sunxm@mail.buct.edu.cn

1 State Key Laboratory of Chemical Resource Engineering, Beijing Advanced Innovation Center for Soft Matter Science and Engineering, Beijing University of Chemical Technology, Beijing 100029, People's Republic of China

2 Shandong University of Science and Technology, Electrical Engineering and Automation, Tsingtao 266590, People's Republic of China

3 Department of Chemical Engineering, Loughborough University, Loughborough, Leicestershire LE11 3TU, UK

4 Interdisciplinary Nanoscience Center (INANO), Sino-Danish Center for Education and Research (SDC), Aarhus University, 8000 Aarhus C, Denmark

5 Beijing Synchrotron Radiation Facility, Institute of High Energy Physics, Chinese Academy of Sciences, Beijing 100049, People's Republic of China

HIGHLIGHTS

- Precisely located S doping of atomic Fe-N$_4$ in Fe(N$_3$)(N–C–S) motif was realized.

- This S doping renders weakened *OH binding and faster charge transfer on Fe-N$_4$.

- Fe-NSC showed excellent oxygen reduction reaction performance with onset potential ~ 1.09 V and half-wave potential ~ 0.92 V.

ABSTRACT Immobilizing metal atoms by multiple nitrogen atoms has triggered exceptional catalytic activity toward many critical electrochemical reactions due to their merits of highly unsaturated coordination and strong metal-substrate interaction. Herein, atomically dispersed Fe-NC material with precise sulfur modification to Fe periphery (termed as Fe-NSC) was synthesized, X-ray absorption near edge structure analysis confirmed the central Fe atom being stabilized in a specific configuration of Fe(N$_3$)(N–C–S). By enabling precisely localized S doping, the electronic structure of Fe-N$_4$ moiety could be mediated, leading to the beneficial adjustment of absorption/desorption properties of reactant/intermediate on Fe center. Density functional theory simulation suggested that more negative charge density would be localized over Fe-N$_4$ moiety after S doping, allowing weakened binding capability to *OH intermediates and faster charge transfer from
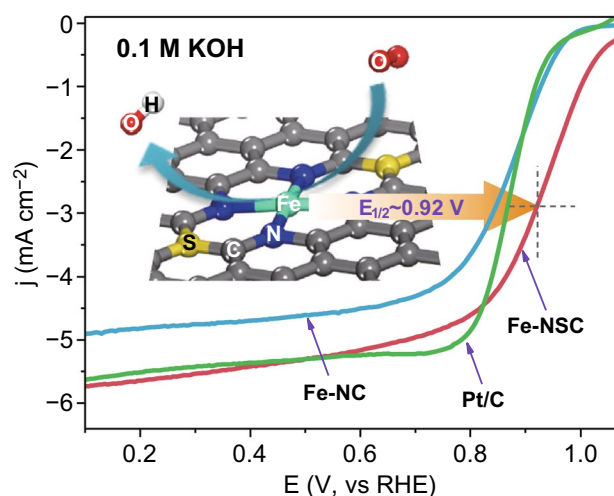
Fe center to O species. Electrochemical measurements revealed that the Fe-NSC sample exhibited significantly enhanced oxygen reduction reaction performance compared to the S-free Fe-NC material (termed as Fe-NC), showing an excellent onset potential of 1.09 V and half-wave potential of 0.92 V in 0.1 M KOH. Our work may enlighten relevant studies regarding to accessing improvement on the catalytic performance of atomically dispersed M-NC materials by managing precisely tuned local environments of M-N_x moiety.

KEYWORDS Atomic dispersion; Iron–nitrogen moiety; Electronic structure; Sulfur doping; Oxygen reduction

1 Introduction

Atomically dispersed metal-nitrogen-carbon (M-NC) materials have received considerable attention due to excellent catalytic performance that boost sustainable and clean energy utilization technologies such as fuel cells [1–3], metal-air batteries [4–6], water electrolyzers [7–9], CO_2/N_2 fixation [10–13]. Their exceptional catalytic performance, as has been extensively studied, is firstly owing to the isolation presence of metal atom in high unsaturated coordination and high surface energy, secondly thanks to the strong beneficial interaction effects between atomic metal center and conductive substrate [14–17]. Besides of stabilizing metal centers via M-N_4 moiety, the multiple N atoms surrounding metal center also act as bridges for communicating electrons in and out of metal centers and coordinators for responding the feedback from active substrate [18–21]. Therefore, it is of great importance and flexibility to tune the catalytic properties of central metal sites by simply manipulating the configuration and functionality of the coordinated N species.

Nowadays, most researches regarding atomically dispersed M-NC materials are being focused on the characterizations of active sites by using cutting-edge characterization techniques [22–25], and developments of new types of metal centers to fit more applicable fields [26–29], leaving large space for finely tuning the electronic properties of M-N_x moieties via local heteroatom doping. Currently, there have been some literatures reporting that the catalytic performance of atomically dispersed M-NC materials is highly related with rational design and optimization of the atomic structures of M-N_x moieties through adjusting their electronic properties, such as by breaking symmetry with $x \neq 4$ [30–32], doping metal center or N periphery with heteroatoms [33–36]. However, it is still a big challenge to achieve optimal heterodoping through the trial-and-error introduction of heteroatom sources into starting materials. In order to achieve controllable dispersion of heteroatom dopants, distinct coupling and doping routes to the near adjacency of M-N_x moiety and clear understanding of

heteroatom doping effects on the catalytic performance of M-N_x moiety are urgently called for.

Herein, the chemistry between formamide (N and C source) and thiourea (S source) was engaged to realize the local S doping to the atomically dispersed Fe–N_4 moieties. The location of S atoms is confirmed by X-ray absorption near edge structure (XANES) analysis and Fe K-edge fitting in a configuration of Fe(N_3)(N–C–S), which was inherited from the Shiff-base reaction pathway between amino groups on thiourea and carbonyl group on formamide [37]. Electrochemical measurements revealed that the S-doped atomically dispersed Fe-NC (shorted as Fe-NSC) material delivered excellent onset potential (~ 1.09 V) and half-wave potential (~ 0.92 V) for oxygen reduction reaction (ORR) in alkaline electrolyte. The significantly enhanced catalytic performance of Fe-NSC relative to S-free Fe-NC, in the first place, was ascribed to the isolated exposure of Fe atoms and in the second, was owing to the optimally regulated electronic structure by precisely doped S species. Density functional theory (DFT) computation suggested that more charge density would be accumulated around Fe(N_3)(N–C–S) moiety relative to clean Fe-N_4 moiety, which allowed weaker binding capability to *OH intermediates and faster charge transfer from Fe center to O species, thus leading to the enhancement of ORR performance.

2 Experimental

2.1 Materials

Formamide (FA, purity > 99%) was purchased from Xilong Chemical Co., Ltd. Zinc chloride ($ZnCl_2$) and ferric chloride ($FeCl_3$·$4H_2O$) were purchased from Tianjin Fuchen Chemical Research Factory. Sulfuric acid (H_2SO_4, 95-98 wt %), and nitric acid (HNO_3, 65 wt%) were purchased from Sinopharm Chemical Reagent Co., Ltd. N,N-dimethylformamide (DMF, purity > 99.5%) and thiourea (purity > 99.0%) were purchased from Aladdin reagent Co., Ltd. The commercial

Pt/C catalyst (20 wt%, ~ 3 nm Pt nanoparticles on Vulcan XC-72 carbon support) was purchased from Shanghai Mack-Lin biochemical technology co. LTD. Nafion/water or ethanol solution (~ 5 wt%) was purchased from Sigma-Aldrich Co., LTD. All chemicals were used as received without further purification.

2.2 Preparations of Fe-NSC Material

The precursor for the preparation of Fe-NSC was synthesized via solvothermal method. In a typical synthesis [37], 0.005 mol L^{-1} $FeCl_3.4H_2O$ (0.035 g), 0.01 mol L^{-1} thiourea (0.012 g), 0.1 mol L^{-1} $ZnCl_2$ (0.408 g), and 30.0 mL formamide (FA) were mixed and sonicated for 30 min to get a homogeneous solution. Then, the mixture was transferred to autoclave and heated at 180 °C for 12 h. The as-formed brown precipitate was membrane-filtered, purified with deionized water 3 times and dried at 60 °C overnight. Then, the dried precursor was grinded in quartz mortar and heated to 900 °C for 2 h at a heating rate of 5 °C min^{-1} under Ar flow protection. The synthesis of control sample Fe-NC is like the Fe-NSC except for adding no thiourea.

2.3 Characterizations

Transmission electron microscopy (TEM) images were recorded by a Hitachi-7700 operating at 100 kV. High-resolution transmission electron microscopy (HRTEM, operated at 200 kV) images were recorded using a JEOL 2100 high-resolution transmission electron microscope. High-angle annular dark field-scanning transmission electron microscope (HAADF-STEM) images and corresponding element mapping images were recorded on a JEOL JEM-ARM200F TEM/STEM with a spherical aberration corrector (operated at 300 kV). Powder X-ray diffraction (XRD) patterns were recorded from 5 to 80° at a scan rate of 10° min^{-1} using the Cu Kα 1.5406 Å radiation (MeasSrv F9XDZ42). Raman spectra were recorded on a LabRAM Aramis Raman spectrometer (HORIBA Jobin–Yvon, 500–3000 cm^{-1}) with 532 nm line of Ar laser as excitation source. X-ray photoelectron spectroscopy (XPS) was recorded on a Thermo Electron ESCALAB250 XPS Spectrometer.

XAFS measurement and data analysis: XAFS spectra at the Fe K-edge were measured at the beamline 1W1B station of the Beijing Synchrotron Radiation Facility (BSRF), China. The Fe K-edge XAFS data of Fe-NSC were recorded in a fluorescence mode. Fe foil, FePc, and Fe_2O_3 were used as references in a transmission mode. The acquired EXAFS data were processed with the ATHENA module. The k^3-weighted EXAFS spectra in the k-space ranging from 2 to 10.5 $Å^{-1}$ were Fourier-transformed to real (R) space using a Hanning windows. The data fitting was done with Artemis software.

2.4 Electrochemical Measurements

The working electrode was prepared by ultrasonically mixing 5.0 mg of catalyst sample with the mixture of 490 μL DMF and 10 μL 5% Nafion solution for 30 min to form homogeneous catalyst ink, and then, certain volume of the catalyst ink was cast-dropped onto polished glassy carbon rotating disk electrode (RDE, diameter ~ 5 mm) with a catalyst loading of 0.254 mg cm^{-2}. The catalyst-modified RDE was submitted to electrochemical measurement of catalyzing ORR in both acid (0.1 mol L^{-1} $HClO_4$) and alkaline electrolytes (0.1 mol L^{-1} KOH). Electrochemical measurements were carried out in a three-electrode setup on a Pine Modulated Speed Rotator with WaveDrive10 electrochemical workstation. Before ORR measurements, the O_2 gas was bubbled into the electrolyte for at least 30 min to form O_2 saturation. The cyclic voltammetry (CV) was collected at scan rate of 10 mV s^{-1}. The polarization curves of ORR were collected at rotation speed of 400, 625, 900, 1225, 1600, and 2025 rpm with a scan rate of 5 mV s^{-1}. The transferred electron number (n) and kinetic current density (J_K) were calculated from the Koutecky–Levich equation [38]:

$$\frac{1}{J} = \frac{1}{J_L} + \frac{1}{J_K} = \frac{1}{B\omega^{1/2}} + \frac{1}{J_K} \qquad (1)$$

$$B = 0.62nFC_0D_0^{2/3}v^{-1/6} \qquad (2)$$
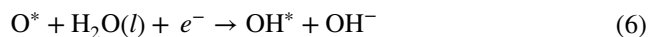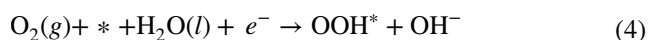
$$J_K = \frac{1}{nKFC_0} \qquad (3)$$

where J is the measured current density; J_K and J_L are the kinetic and limiting current densities, respectively; ω is the angular velocity of the disk; n is the transferred electron number; F is the Faraday constant (96,485 C mol^{-1}); C_0 is the bulk concentration of O_2 (1.2×10^{-6} mol cm^{-3} in 0.1 mol L^{-1} KOH, and 1.26×10^{-6} mol cm^{-3} in 0.1 mol L^{-1} $HClO_4$),

D_0 is the diffusion coefficient of O_2 (1.9×10^{-5} cm^2 s^{-1} in 0.1 mol L^{-1} KOH and 1.93×10^{-5} cm^2 s^{-1} in 0.1 mol L^{-1} HClO$_4$); and υ is the kinematic viscosity of the electrolyte (0.01 cm^2 s^{-1} in 0.1 mol L^{-1} KOH and 1.009×10^{-2} cm^2 s^{-1} in 0.1 mol L^{-1} HClO$_4$). All the constants are data at 1 atm. and 25 °C.

2.5 Calculation Models and Mechanism

Material Studio 5.5 software package was utilized to construct all the three Fe-NSC models based on a periodic 4×4 graphene monolayer for the carbon framework. Subsequently, two carbon atoms were removed, followed by the substitution of four carbon atoms around the divacancy site with four nitrogen atoms to provide the anchoring site for iron atom. The carbon atoms adjacent to and opposite to the central Fe-N$_4$ moiety were replaced by sulfur atoms, respectively, to stimulate the possible Fe-NSC structure, which further confirmed as Fe-NS$_1$C, Fe-NS$_2$C. C–S–C bonds were also considered and regarded as most likely existing state of S based on XPS analysis. Symmetrically, we constructed the existence situation of C–S–C bonds near the center of Fe-N$_4$ moiety and defined it as the third possibility, Fe-NS$_3$C. Oxygen reduction calculations were developed by the Viena Ab initio Simulation Package (VASP), by density functional theory (DFT + U, the description correlation for Fe is 3.5). Generalized Gradient Approximation (GGA) replaced the inner cores and the Perdew–Burke–Ernzerh (PBE) of functional were used to describe the exchange and correlation. The bulk lattice was optimized using the $3 \times 3 \times 3$ Monkhorst–Pack type of K-point sampling with a period slab model for in the space of 16 Å vacuum. The cutoff energy was 400 eV, followed with an energy change convergence criterion of 1×10^{-4} eV. Spin polarization was also considered in all the calculations including the dipole correlation.

The stimulation of ORR process on active center of Fe-NSC was developed in the alkaline electrolyte. Thus, the four-electron transferred pathway, thus, the mechanism of oxygen reduction on single atom site could be normally treated as follows:

$$O_2(g) + * + H_2O(l) + e^- \rightarrow OOH^* + OH^- \tag{4}$$

$$OOH^* + e^- \rightarrow O^* + OH^- \tag{5}$$

$$O^* + H_2O(l) + e^- \rightarrow OH^* + OH^- \tag{6}$$

$$OH^* + e^- \rightarrow * + OH^- \tag{7}$$

The symbol of * stands for the active center which locate on the surface of catalytic bulk, and O*, OH*, and OOH* are adsorbed intermediates in the procedure of electrochemical reaction. Free Gibbs energy change (ΔG) from initial state to final state of oxygen reduction can be calculated as:

$$\Delta G = \Delta E + \Delta ZPE - T\Delta S + \Delta G_U + \Delta G_{pH} \tag{8}$$

where ΔE stands for the reaction energy change of adsorbed reactant and product molecules on the active sites of catalysts, by analyzing the DFT results. ΔZPE and ΔS are the changes of zero-point energies and entropy due to the reaction, respectively. The ΔG_U shows the applied potential change relative to RHE, and ΔG_{pH} is the correction for H$^+$ free energy.

3 Results and Discussion

3.1 Characterization of Fe-NSC

As shown in Fig. 1a, the S-doped atomically dispersed Fe-NC materials, termed as Fe-NSC, were prepared via consecutive steps of solvothermal treatment and inert annealing. Formamide (FA) and thiourea molecules were utilized as C/N and S sources, respectively. During the solvothermal treatment, FA molecules crosslink via Shiff-base reaction to form multi-dentate polymeric ligands for anchoring ionic Fe^{3+} and Zn^{2+} [37]. In the meantime, thiourea molecules are able to incorporate to the neighbor of Fe-(N–C)$_4$ moieties via Shiff-base reaction pathway between FA and thiourea. During the second step of high temperature annealing at 900 °C in N$_2$ flow, carbothermic-reduced Zn substance vaporizes (boiling point of Zn is 906 °C), accompanying with the removal of unstable organic functionalities to reach high carbonization/graphitization degree [39]. Eventually, the targeted Fe-NSC material with atomically dispersed Fe sites, stable N$_4$ surrounding, and S doping to the N$_4$ moieties is obtained, as confirmed later in the section of XANES analysis. Therefore, our method based on FA chemistry may enable the adjustment on the charge density of atomic Fe center through N coordinators and surrounded S atoms.

The morphology of Fe-NSC was first probed using TEM and high-angle annular dark field-scanning transmission
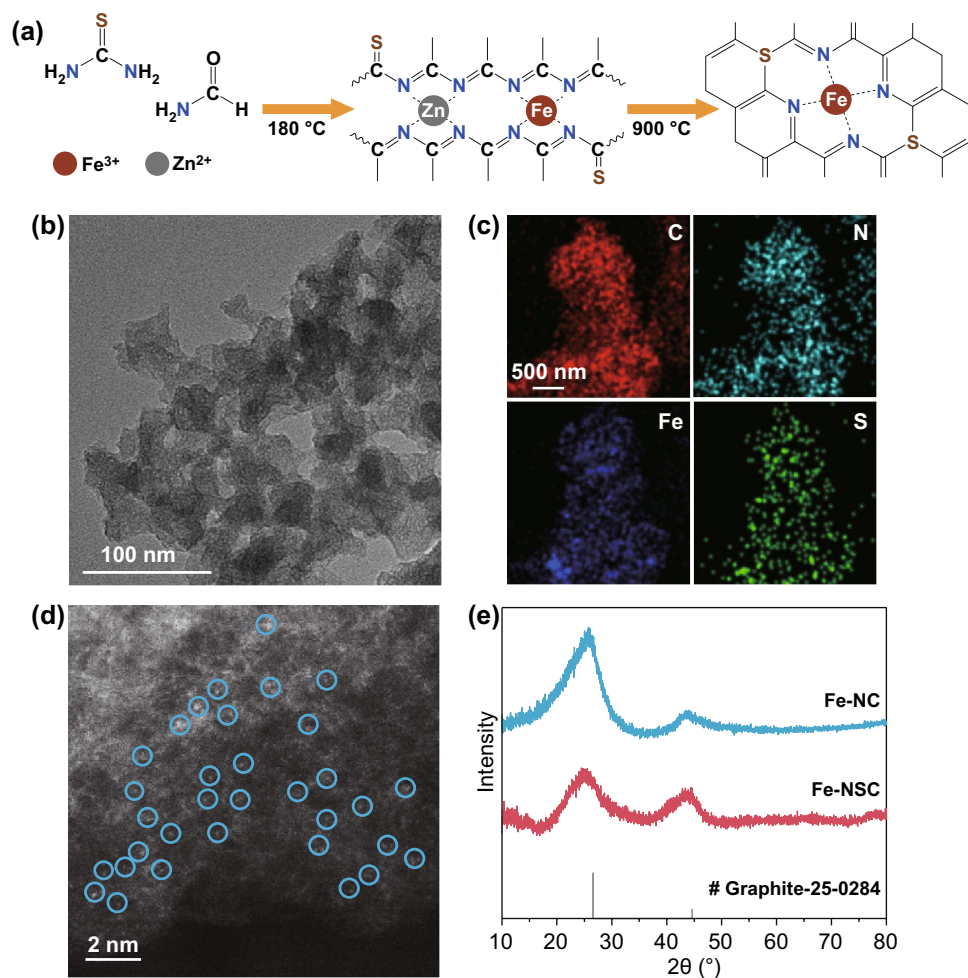
Fig. 1 **a** Schematic illustration of the synthesis of Fe-NSC. **b** HRTEM and **c** element mapping images of Fe-NSC, **c** the uniform distribution of C (red), N (cyan), Fe (blue), and S (green) elements. **d** HAADF-STEM image of Fe-NSC, bright dots corresponds to the atomically dispersed Fe atoms. **e** XRD profiles of Fe-NC and Fe-NSC

electron microscope (HAADF-STEM). The HRTEM image of Fe-NSC material in Fig. 1b shows even contrast, and no Fe aggregate is observed, implying the Fe components maintaining in cluster or possibly atomic dispersion. Meanwhile, the corresponding elemental mapping images confirm the uniform distribution of C, Fe, N, and S throughout the as-made Fe-NSC material (Fig. 1c). As indicated by the bright dots marked with circles (Fig. 1d), the HAADF-STEM image then confirms the Fe components in atomic dispersion in the N, S-codoped carbon matrix. Besides, no Fe aggregate and Fe components in atomic dispersion are seen in the control sample of Fe-NC obtained without thiourea (Fig. S1a, b), which mainly owes to the effects of Zn fencing and surrounding N immobilizing [40, 41].

The Fe-NSC and Fe-NC materials were further examined using XRD and Raman. As shown in Fig. 1e, the XRD profiles of Fe-NSC and Fe-NC exhibit two characteristic peaks at approximately 26.2° and 46.3°, which are indexing to the (002) and (100) plane of graphitic carbon, respectively. There is no diffraction additional peak observed that can be indexed to Fe-based compound or Fe substance for both Fe-NSC and Fe-NC, which agrees with HRTEM and STEM data, implying Fe components in high dispersion. Raman spectra (Fig. S1c) of Fe-NC and Fe-NSC show two evident bands locate at ~ 1352 and ~ 1591 cm^{-1} that, respectively, attribute to the D band (dispersive defect-induced vibration) and G band (the vibration of sp^2-bonded carbon atoms) [42–44], indicating the high carbonization/graphitization

feature of Fe-NSC and Fe-NC samples. The N_2 adsorption/desorption measurement was employed to reveal the specific surface areas (SSA) and pore structures of Fe-NSC and Fe-NC. As indicated by the N_2 adsorption and desorption (A/D) isotherms in Fig. S2a, both Fe-NSC and Fe-NC contain large amount of micropores and macropores, and small amount of mesopores that together build hierarchically porous structure. The BET SSA of Fe-NSC and Fe-NC are calculated to be 531.9 and 421.0 m^2 g^{-1}, respectively. The larger SSA of Fe-NSC implies that S doping could possibly induce more defects and structure distortion [44, 45]. Pore distribution curves are calculated using DFT method and showed in Fig. S2b, and it confirms the presence of considerable amounts of micropores and macropores presenting in both Fe-NSC and Fe-NC. Hierarchical porosity has been confirmed beneficial for facilitating electrolyte penetration and mass transportation in electrode materials [46–49].

X-ray photoelectron spectroscopy (XPS) was employed to analyze the composition of Fe-NSC and Fe-NC. XPS element surveys confirm the common presence of C, N, O, Fe elements in both Fe-NSC and Fe-NC (Fig. S3a), and Fig. 2a summarized the details of element contents in Fe-NSC and Fe-NC (see also in Table S1), in which Fe-NSC contains 77.71 at% C, 7.36 at% N, 0.86 at% Fe, and 2.07 at% S. In contrast, Fe-NC contains 85.80 at% C, 5.29 at% N, and 0.60 at% Fe. Detailed deconvolution of C 1s, N 1s, Fe 2p, and S 2p spectra was performed. Figure S3b reveals that more C–N and C–S connections are presenting in Fe-NSC than in Fe-NC, which is in accordance with element survey. With S introduction, more anchorable N atoms would stay in six-atom ringed pyridinic configuration (binding energy centered at ~ 398.5 eV) than in five-atom ringed pyrrolic form (binding energy centered at ~ 399.6 eV) (Fig. 2b) [50]. The XPS Fe 2p spectra in Fig. 2c show that both the Fe2$p^{3/2}$ branches for Fe-NSC and Fe-NC spanning from 708 to 714 eV, suggesting the Fe components most likely presenting in their oxidative states. It is noteworthy that the band center of Fe-NSC shows approximately 0.5 eV blue-shifted compared to Fe-NC, meaning that the Fe atoms in Fe-NSC are in more reductive state, which is probably due to the
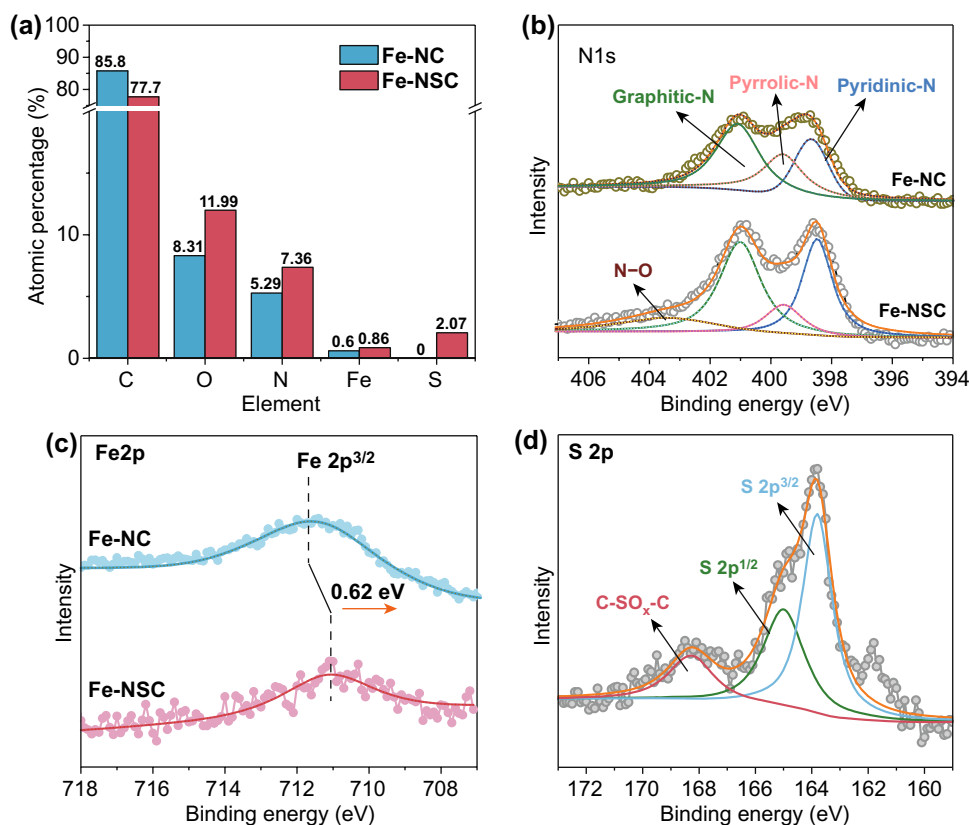

Fig. 2 XPS analysis of Fe-NSC and Fe-NC. **a** Element contents, fine scans on **b** Fe 2p spectra, **c** N 1s spectra, and **d** S 2p spectra

close incorporation of S atom [51]. As shown in Fig. 2d, there are two main peaks located at ~ 164.0 and ~ 165.1 eV for the S species in Fe-NSC, which can be ascribed to the S $2p^{3/2}$ and S $2p^{1/2}$ branches of C-S-C moieties, and a minor peak centered at ~ 168.5 eV can be attributed to the sulfate species (–C–SO$_x$–C, x = 1 or 2) [52–54].

The K-edge EXAFS of Fe-NSC and Fe-NC materials were measured to obtain deep insight into the local structures of

active sites [55]. The N K-edge XANES spectra (Fig. 3a) reveal that the π^* resonances at ~ 398, ~ 400.1, and 401.6 eV can be ascribed to the ringed structure consisting of pyridinic N, pyrrolic N, and quaternary N, respectively. The band at ~ 407.4 eV can be attributed to the σ^* of C–N–C or C–N bonding [56, 57]. The Fe-NSC shows more evident π^* resonance band at 400.1 eV, suggesting higher pyrrolic N content, which is in good agreement with XPS analysis.
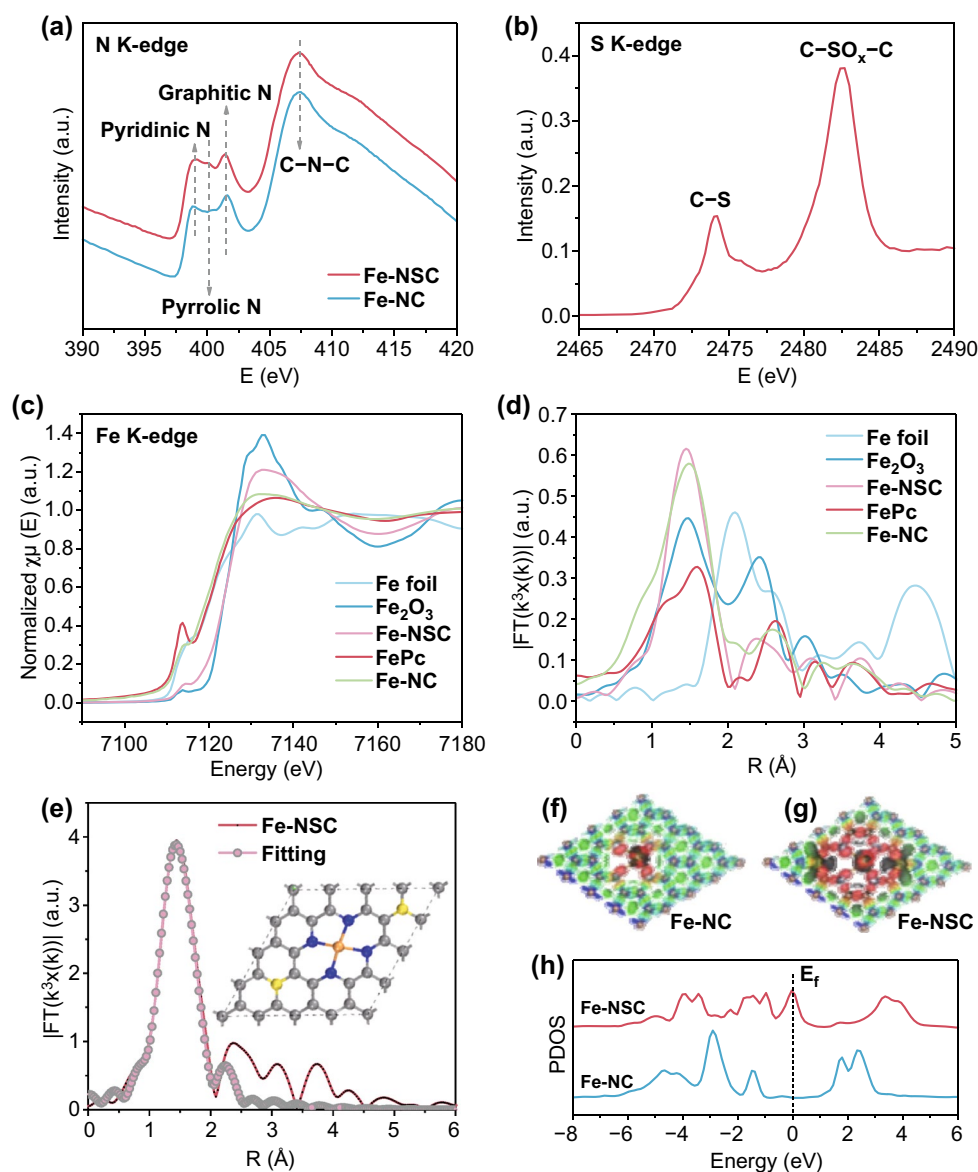

Fig. 3 **a** N K-edge for Fe-NSC and Fe-NC, **b** S K-edge for Fe-NSC, and **c** experimental K-edge XANES Fe spectra of Fe-NSC, Fe-NC, and reference samples (Fe foil, FePc, and Fe$_2$O$_3$). **d** Fourier-transformed (FT) k^3-weighted χ(k)-function of the EXAFS spectra for Fe K-edge of Fe-NSC, Fe-NC, and reference samples. **e** Corresponding Fe K-edge EXAFS fitting curves of Fe-NSC in R space, inset shows the proposed structure of Fe-N4 with local S doping. Top view of the charge densities of **f** Fe-NC (left) and **g** Fe-NSC (right), red area represents electron accumulation. **h** Partial density of states (DOS) for Fe d band in Fe-NSC and Fe-NC

The S K-edge XANES (Fig. 3b) presents two typical peaks at 2474.2 and 2482.6 eV that can be indexed to C–S–C and C–SO$_x$–C bonding, confirming the achievable S doping in Fe-NSC. The Fe K-edge XANES spectrum of Fe-NSC indicates its energy absorption threshold locating to the right of Fe-NC, Fe foil, and FePc, and closer to that of Fe$_2$O$_3$, implying the more positively charged Fe$^{\delta+}$ ($2 < \delta < 3$) in Fe-NSC than in Fe-NC (Fig. 3c) [58]. FT-EXAFS spectrum (Fig. 3d) of Fe-NSC at Fe K-edge exhibits only one major peak at ~1.45 Å and no Fe–Fe bonding at ~2.09 Å, confirming the scattering Fe-N path. EXAFS fitting was performed to further manifest the coordination structure of Fe-N paths (Figs. 3e, S4 and Table S2) [57]. The fitting result shows that each Fe atom is coordinated by average four N atoms, giving the estimated structure of Fe-N$_4$ with S doping at the S–C–N–Fe, as shown in the inset of Fig. 3e.

DFT study was conducted to identify the beneficial effect of neighboring S on Fe-N$_4$ moiety. Firstly, the charge distribution and partial density of states (PDOS) were established by using a model with Fe-N$_4$ sites embedded in N, S-co-doped carbon substrate to mimic the active sites of S-neighbored Fe-N$_4$ moiety in Fe-NSC, as shown in Fig. 3f, g. Compared to that of Fe-NC, the charge distribution pattern of Fe-NSC shows strong electron accumulation (marked by red area) around Fe center. The extended electron accumulation around Fe-N$_4$ moiety is attributed to neighboring S regulation, leading to more electron density partially accumulated on Fe centers [51]. The denser charge density of Fe-N$_4$ moiety promoted by S regulation may help to accelerate charge transfer during ORR processes [59, 60]. The PDOS of Fe atoms in Fe-NSC and Fe-NC indicate that the gap of Fe d band in Fe-NSC structure is much narrower than that in Fe-NC (Fig. 3h), meaning S doping in Fe-NC also contributing the improvement on conductivity. Moreover, the highly localized d band center of Fe in Fe-NSC are up-shifted with reduced intensity, which leads to weaker binding capability to reactant O$_2$ molecules and better electron transferring [59]. These above DFT simulation results strongly suggest that the electronic structure of Fe-N$_4$ moieties has been efficiently regulated by neighboring S [61, 62].

3.2 ORR Performance of Fe-NSC

The as-obtained Fe-NSC, Fe-NC, and 20 wt % Pt/C (Pt/C) were submitted to ORR measurements. Their catalytic activity was first investigated by using cyclic voltammetry (CV) and linear sweep voltammetry (LSV) measurements in O$_2$-saturated 0.1 mol L^{-1} KOH with the same catalyst loading of 0.254 mg cm^{-2}. It is notable in the CV profiles (Fig. 4a) that Fe-NSC exhibits a remarkably high peak-current potential of 0.82 V at scan rate of 100 mV s^{-1}, while the Fe-NC and Pt/C show lower peak-current potentials of 0.78 and 0.74 V, respectively. As examined by LSV, the onset potential of Fe-NSC is ~1.09 V, which largely surpasses those of Pt/C and Fe-NC for over 90 and 80 mV, respectively (Fig. 4b), which agrees with their corresponding CV curves. The achieved high onset potential of 1.09 V for ORR in alkaline is among the best values ever reported (Table S3). Meanwhile, the Fe-NSC catalyzed ORR shows an exceptional half-wave potential ($E_{1/2}$) of 0.92 V in 0.1 mol L^{-1} KOH (inset of Fig. 4b), which is 50 and 70 mV positive compared to those of Pt/C (~0.87 V) and Fe-NC (~0.85 V). The electron transfer number (n) of Fe-NSC and Fe-NC was measured using LSV curves obtained at different rotation speeds with a scan rate of 5 mV s^{-1} (Fig. S5a, c). As displayed in Fig. S5b, the linearity of the Koutecky–Levich (K-L) plots of Fe-NSC indicates the first-order reaction kinetics and the n was calculated to be ~4.0 at the potential range of 0.2–0.7 V, which is slightly higher than Fe-NC (~3.8) (inset of Fig. 4b). Tafel plots were organized and displayed in Fig. S5e to further investigate the ORR kinetics [63]. The Fe-NSC, Fe-NC, and Pt/C, respectively, reach slopes of 102.8, 103.4, and 106.8 mV dec^{-1}, suggesting the process of O$_2$ to OOH* being determinant at such potential range [49]. The stability toward methanol crossover was investigated by using chronoamperometric technique [64]. A slight current oscillation is observed for Fe-NSC, leading to over 94.0% current retention, indicating good capability to tolerate methanol (Fig. S5f). By contrast, Pt/C exhibits sharp current drop to 38.8% at the moment of methanol injection and is not able to recover after the next 10 min. Electrochemical surface area (ECSA) of both samples was calculated based on their electrochemical double-layer capacitances (EDLCs). As shown in Fig. S6a–c, the Fe-NSC sample possesses a little bit larger ECSA of 8.6 mF cm^{-2} compared to the Fe-NC (~7.4 mF cm^{-2}). We then normalized the specific kinetic current density of ORR using the ECSA, as displayed in Fig. S6d. This bar chart comparison shows that the kinetic current densities of Fe-NSC at three given potentials (0.60, 0.65, and 0.70 V) are higher than those of Fe-NC, further
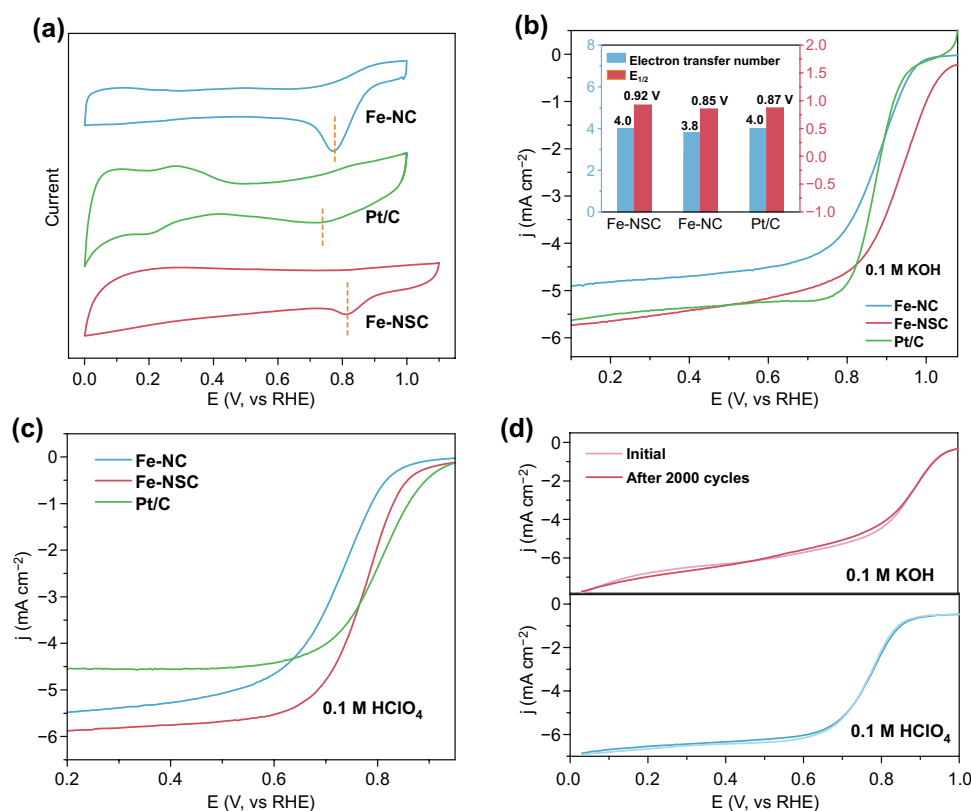
Fig. 4 Electrochemical measurements on Fe-NSC, Fe-NC, and Pt/C. **a** CV profiles with scan rate of 100 mV s^{-1}. LSV curves in O$_2$-saturated **b** 0.1 M KOH and **c** 0.1 M HClO$_4$ with a sweep rate of 5.0 mV s^{-1} and 1600 rpm. **d** Stability test of Fe-NSC in 0.1 M KOH (top) and 0.1 M HClO$_4$ (bottom) for 2000 cycles (~12 h)

confirming the beneficial effect of S introduction to the adjacence of Fe-N$_4$ moiety.

The ORR performance of Fe-NSC, Fe-NC and Pt/C in acidic electrolyte of 0.1 M HClO$_4$ was also studied. Figure S7a shows their CV curves in acid electrolyte, manifesting the very close peak potential of ~0.67 V at peak current for Fe-NSC and Pt/C. The Fe-NSC exhibits an estimated $E_{1/2}$ of 0.78 V, approaching to that of Pt/C (~0.80 V), as compared in Fig. 4c, which is 70-mV positive than that of S-free Fe-NC. Meanwhile, the Fe-NSC shows much larger limiting current density relative to that of Pt/C. Figure S7c shows the n of Fe-NSC that is calculated from LSV curves in Fig. S7b to be ~3.9, implying a near direct 4-electron pathway [65]. Figure S7d reveals that the lowest Tafel slope of 92.6 mV dec^{-1} is achieved by the Fe-NSC over Pt/C (~102.9 mV dec^{-1}) and Fe-NC (~100.2 mV dec^{-1}). In addition, the long-term cycling stability in both alkaline and acidic electrolytes was investigated by using chronoamperometric technique. As shown in Fig. 4d, very limited

activity decays were observed in both alkaline and acid electrolytes for non-stop 12-h working, further supporting that Fe-NSC material is reasonably good ORR catalyst that can be potentially used for proton exchange membrane fuel cell[3]. Furthermore, HRTEM images of Fe-NSC catalyst after 12-h long working were collected and showed in Fig. S8, and no metal aggregates are seen which confirm the Fe-N$_4$ sites are well-reserved in their original atomic dispersion after durability tests.

3.3 DFT Calculations

We simulated another two possible locations of S doping to the periphery of Fe-N$_4$ moiety, and DFT calculations were employed to investigate the adsorption free energy of ORR steps, as well as to evaluate the difference of electronic structures with different S locations. Figure 5a–c displays three S location to Fe-N$_4$ moiety, they are nominated as Fe-NS$_1$C,
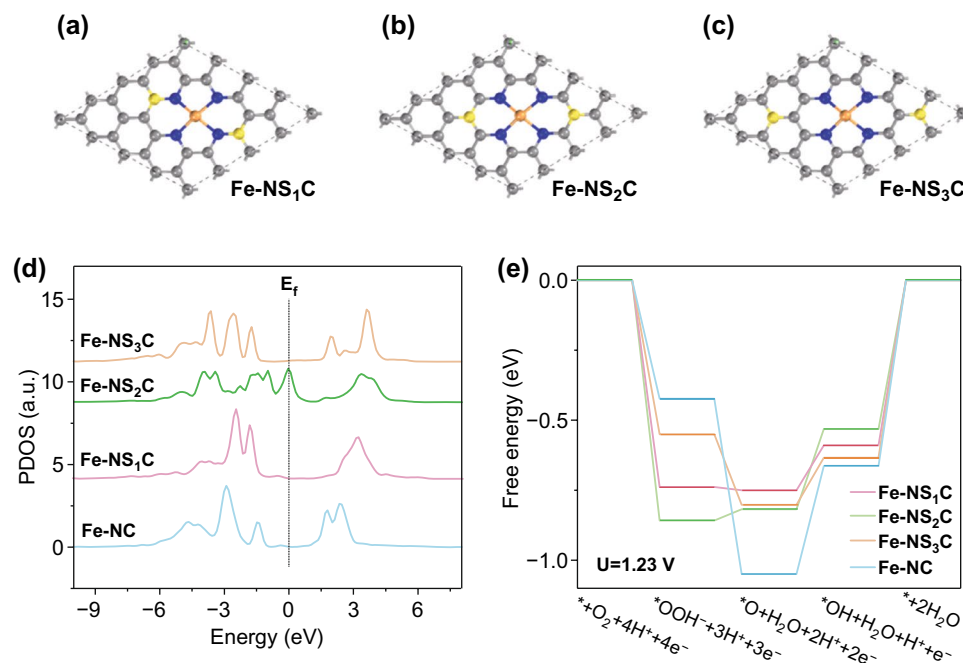
Fig. 5 Top view of atomic structure of Fe-NSC with different S positions: **a** Fe-NS$_1$C, **b** Fe-NS$_2$C, and **c** Fe-NS$_3$C. **d** Partial density of states (PDOS) of Fe d band in Fe-NSC with S doping at different local positions, with comparison to that of Fe-NC. **e** Free-energy diagram of ORR occurring on Fe-NSC with S doping at different local positions, obtained from DFT calculation

Fe-NS$_2$C, and Fe-NS$_3$C according to their positions, and the subscript of S stands for the number sequence next to N-Fe. The projected PDOS of Fe atoms in Fe-NS$_1$C, Fe-NS$_2$C, Fe-NS$_3$C, and Fe-N$_4$C moieties are compared in Fig. 5d. The PDOS study on Fe atom in Fe-NS$_x$-C suggested that the d band gap of Fe in Fe-NS$_2$-C was much narrower than the Fe atoms in other Fe-NS$_x$-C, which can be interpreted into the improved local electronic conductivity in Fe-N$_4$ moiety by adjacent S doping. Figure S9 shows the geometry of each intermediates on Fe site in Fe-NS$_3$C moiety during oxygen reduction catalysis. The free-energy diagrams of ORR promoted by Fe-NS$_1$C, Fe-NS$_2$C, Fe-NS$_3$C, and Fe-NC are displayed in Fig. 5e. All the free-energy calculations were performed at U = 1.23 V for four-electron transfer reactions for oxygen reduction. In the first step of *O$_2$ to *OOH, all the Fe-NS$_x$C (x = 1, 2, or 3) show much larger energy release than Fe-N$_4$ does, confirming their weaker binding capability to O$_2$ molecule. The last step of ORR (*OH reduction) is revealed to be the most sluggish endothermic process and thus can be confirmed to be one rate-determining step (RDS) for both Fe-NSC and Fe-NC catalysts [66]. The overpotential of ORR promoted by Fe-NS$_2$C is calculated to be 0.53 V, which 0.13 V lower than that by Fe-NC, and

this improvement is likely contributed by S doping which reduced the adsorption capacity of *OH intermediate, thus facilitating the dynamic progress of ORR [36].

4 Conclusions

In summary, we have developed a reliable strategy to boost the ORR performance of atomically dispersed Fe-N$_4$ active sites by precise S local doping. The Fe-NSC material has been thoroughly characterized by XRD, XPS, HAADF-STEM, and XANES techniques, confirming the atomically dispersion of Fe component in S-neighbored Fe-N$_4$ structure of Fe(N$_3$)(N–C–S). The significant enhancement of ORR activity of Fe-NSC was confirmed by electrochemical measurements, exhibiting a remarkably high onset potential of 1.09 V and a $E_{1/2}$ of 0.92 V in 0.1 M KOH, which were 90 and 50 mV higher than that of Pt/C, respectively. Meanwhile, the Fe-NSC showed highly comparable acidic ORR performance relative to Pt/C, delivering a 0.78 V $E_{1/2}$ (only 20 mV less than that of Pt/C). The drastically improved ORR activity, as proved by DFT simulations, can be credited to the S doping-induced charge enrichment in N and Fe for optimal O$_2$ binding and fast electron transferring. Our work, beside

of rendering superior ORR catalyst in both alkaline and acid electrolytes, provided a feasible strategy of regulating the local electronic structure of M-N_4 moiety by controllable doping with heteroatoms to improve catalytic performance.

Electronic supplementary material The online version of this article (https://doi.org/10.1007/s40820-020-00456-8) contains supplementary material, which is available to authorized users.

References

1. L. Chen, X. Liu, L. Zheng, Y. Li, X. Guo et al., Insights into the role of active site density in the fuel cell performance of Co–N–C catalysts. Appl. Catal. B **256**(5), 117849 (2019). https://doi.org/10.1016/j.apcatb.2019.117849

2. L. Wang, X. Wan, S. Liu, L. Xu, J. Shui, Fe–N–C catalysts for PEMFC: progress towards the commercial application under DOE reference. J. Energy Chem. **39**, 77–87 (2019). https://doi.org/10.1016/j.jechem.2018.12.019

3. X. Wan, X. Liu, Y. Li, R. Yu, L. Zheng et al., Fe–N–C electrocatalyst with dense active sites and efficient mass transport for high-performance proton exchange membrane fuel cells. Nat. Catal. **2**(3), 259–268 (2019). https://doi.org/10.1038/s41929-019-0237-3

4. J. Wang, W. Liu, G. Luo, Z. Li, C. Zhao et al., Synergistic effect of well-defined dual sites boosting the oxygen reduction reaction. Energy Environ. Sci. **11**(12), 3375–3379 (2018). https://doi.org/10.1039/c8ee02656d

5. Z. Li, H. He, H. Cao, S. Sun, W. Diao et al., Atomic Co/Ni dual sites and Co/Ni alloy nanoparticles in N-doped porous Janus-like carbon frameworks for bifunctional oxygen electrocatalysis. Appl. Catal. B **240**, 112–121 (2019). https://doi.org/10.1016/j.apcatb.2018.08.074

6. Y. Lian, W. Yang, C. Zhang, H. Sun, Z. Deng et al., Unpaired 3d electron on atomically dispersed cobalt centre in coordination polymers to regulate both orr activity and selectivity. Angew. Chem. Int. Ed. **132**(1), 292–300 (2019). https://doi.org/10.1002/ange.201910879

7. L. Zhang, Y. Jia, G. Gao, X. Yan, N. Chen et al., Graphene defects trap atomic Ni species for hydrogen and oxygen evolution reactions. Chem **4**(2), 285–297 (2018). https://doi.org/10.1016/j.chempr.2017.12.005

8. F. Li, G.-F. Han, H.-J. Noh, J.-P. Jeon, I. Ahmad et al., Balancing hydrogen adsorption/desorption by orbital modulation for efficient hydrogen evolution catalysis. Nat. Commun. **10**(1), 4060 (2019). https://doi.org/10.1038/s41467-019-12012-z

9. Y. Hou, M. Qiu, M.G. Kim, P. Liu, G. Nam et al., Atomically dispersed nickel–nitrogen–sulfur species anchored on porous carbon nano-sheets for efficient water oxidation. Nat. Commun. **10**(1), 1392 (2019). https://doi.org/10.1038/s41467-019-09394-5

10. L. Han, X. Liu, J. Chen, R. Lin, H. Liu et al., Atomically dispersed molybdenum catalysts for efficient ambient nitrogen fixation. Angew. Chem. Int. Ed. **58**(8), 2321–2325 (2019). https://doi.org/10.1002/ange.201900203

11. P. Huang, M. Cheng, H. Zhang, M. Zuo, C. Xiao, Y. Xie, Single Mo atom realized enhanced CO_2 electro-reduction into formate on n-doped graphene. Nano Energy **61**, 428–434 (2019). https://doi.org/10.1016/j.nanoen.2019.05.003

12. D. Karapinar, N.T. Huan, N.S. Ranjbar, J. Li, D. Wakerley et al., Electroreduction of CO_2 on single-site copper-nitrogen-doped carbon material: selective formation of ethanol and reversible restructuration of the metal sites. Angew. Chem. Int. Ed. **58**(42), 15098–15103 (2019). https://doi.org/10.1002/ange.201907994

13. H. Zhang, Y. Liu, T. Chen, J. Zhang, J. Zhang, X.W.D. Lou, Unveiling the activity origin of electrocatalytic oxygen evolution over isolated ni atoms supported on a N-doped carbon matrix. Adv. Mater. **31**(48), 1904548 (2019). https://doi.org/10.1002/adma.201904548

14. A.S. Varela, W. Ju, A. Bagger, P. Franco, J. Rossmeisl, P. Strasser, Electrochemical reduction of CO_2 on metal-nitrogen-doped carbon catalysts. ACS Catal. **9**(8), 7270–7284 (2019). https://doi.org/10.1002/aenm.201703614

15. Q.-Q. Yan, D.-X. Wu, S.-Q. Chu, Z.-Q. Chen, Y. Lin et al., Reversing the charge transfer between platinum and sulfur-doped carbon support for electrocatalytic hydrogen evolution. Nat. Commun. **10**(1), 4977 (2019). https://doi.org/10.1038/s41467-019-12851-w

16. J. Li, Q. Guan, H. Wu, W. Liu, Y. Lin et al., Highly active and stable metal single-atom catalysts achieved by strong electronic metal–support interactions. J. Am. Chem. Soc. **141**(37), 14515–14519 (2019). https://doi.org/10.1021/jacs.9b06482

17. Z. Li, L. Wei, W.-J. Jiang, Z. Hu, H. Luo et al., Chemical state of surrounding iron species affects the activity of Fe-Nx for electrocatalytic oxygen reduction. Appl. Catal. B **251**(15), 240–246 (2019). https://doi.org/10.1016/j.apcatb.2019.03.046

18. S. Büchele, Z. Chen, S. Mitchell, R. Hauert, F. Krumeich, J. Pérez-Ramírez, Tailoring nitrogen-doped carbons as hosts for single-atom catalysts. ChemCatChem **11**(12), 2812–2820 (2019). https://doi.org/10.1002/cctc.201900547

19. J. Li, S. Ghoshal, W. Liang, M.-T. Sougrati, F. Jaouen et al., Structural and mechanistic basis for the high activity of Fe–N–C catalysts toward oxygen reduction. Energy Environ. Sci. **9**(7), 2418–2432 (2016). https://doi.org/10.1039/c6ee01160h

20. K. Strickland, E. Miner, Q. Jia, U. Tylus, N. Ramaswamy et al., Highly active oxygen reduction non-platinum group metal electrocatalyst without direct metal–nitrogen coordination. Nat. Commun. **6**(1), 7343 (2015). https://doi.org/10.1038/ncomms8343

21. N. Zhang, T. Zhou, M. Chen, H. Feng, R. Yuan et al., High-purity pyrrole-type FeN_4 site as superior oxygen reduction electrocatalyst. Energy Environ. Sci. **13**, 111–118 (2020). https://doi.org/10.1039/c9ee03027a

22. Q. Jia, E. Liu, L. Jiao, S. Pann, S. Mukerjee, X-ray absorption spectroscopy characterizations on pgm-free electrocatalysts: justification, advantages, and limitations. Adv. Mater. **31**(31), 1805157 (2018). https://doi.org/10.1002/adma.201805157

23. U.I. Kramm, L. Ni, S. Wagner, 57Fe mössbauer spectroscopy characterization of electrocatalysts. Adv. Mater. **31**(31), 1805623 (2019). https://doi.org/10.1002/adma.201805623

24. X. Li, X. Yang, J. Zhang, Y. Huang, B. Liu, In situ/operando techniques for characterization of single-atom catalysts. ACS Catal. **9**(3), 2521–2531 (2019). https://doi.org/10.1021/acscatal.8b04937

25. S. Wagner, H. Auerbach, C.E. Tait, I. Martinaiou, S.C. Kumar et al., Elucidating the structural composition of a fe-n-c catalyst by nuclear and electron resonance techniques. Angew. Chem. Int. Ed. **58**(31), 10486–10492 (2019). https://doi.org/10.1002/ange.201903753

26. K. Chi, Z. Chen, F. Xiao, W. Guo, W. Xi et al., Maximizing the utility of single atom electrocatalysts on a 3d graphene nanomesh. J. Mater. Chem. A **7**(26), 15575–15579 (2019). https://doi.org/10.1039/c9ta00942f

27. J. Zhang, X. Tian, M. Liu, H. Guo, J. Zhou et al., Cobalt modulated mo-dinitrogen interaction in MoS_2 for catalyzing ammonia synthesis. J. Am. Chem. Soc. **141**(49), 19269–19275 (2019). https://doi.org/10.1021/jacs.9b02501

28. Y. Qu, L. Wang, Z. Li, P. Li, Q. Zhang et al., Ambient synthesis of single-atom catalysts from bulk metal via trapping of atoms by surface dangling bonds. Adv. Mater. **31**(44), 1904496 (2019). https://doi.org/10.1002/adma.201904496

29. V. Ramalingam, P. Varadhan, H.C. Fu, H. Kim, D. Zhang et al., Heteroatom-mediated interactions between ruthenium single atoms and an MXene support for efficient hydrogen evolution. Adv. Mater. **31**(48), 1903841 (2019). https://doi.org/10.1002/adma.201903841

30. H. Zhang, J. Li, S. Xi, Y. Du, X. Hai et al., Graphene supported single-atom FeN5 catalytic site for efficient electrochemical CO2 reduction. Angew. Chem. Int. Ed. **58**(42), 14871–14876 (2019). https://doi.org/10.1002/ange.201906079

31. B. Zhang, J. Zhang, J. Shi, D. Tan, L. Liu et al., Manganese acting as a high-performance heterogeneous electrocatalyst in carbon dioxide reduction. Nat. Commun. **10**(1), 2980 (2019). https://doi.org/10.1038/s41467-019-10854-1

32. A.B. Anderson, E.F. Holby, Pathways for O_2 electroreduction over substitutional FeN_4, $HoFeN_4$, and $OFeN_4$ in graphene bulk sites: critical evaluation of overpotential predictions using lger and che models. J. Phys. Chem. C **123**(30), 18398–18409 (2019). https://doi.org/10.1021/acs.jpcc.9b03703

33. J. Zhang, M. Zhang, Y. Zeng, J. Chen, L. Qiu et al., Single Fe atom on hierarchically porous s, n-codoped nanocarbon derived from porphyra enable boosted oxygen catalysis for rechargeable Zn-air batteries. Small **15**(24), 1900307 (2019). https://doi.org/10.1002/smll.201900307

34. J.-C. Li, H. Zhong, M. Xu, T. Li, L. Wang et al., Boosting the activity of fe-n x moieties in Fe-NC electrocatalysts via phosphorus doping for oxygen reduction reaction. Sci. China Mater. (2019). https://doi.org/10.1007/s40843-019-1207-y

35. H. Sun, M. Wang, X. Du, Y. Jiao, S. Liu et al., Modulating the d-band center of boron doped single-atom sites to boost the oxygen reduction reaction. J. Mater. Chem. A **7**(36), 20952–20957 (2019). https://doi.org/10.1039/c9ta06949f

36. Y. Mun, S. Lee, K. Kim, S. Kim, S. Lee, J.W. Han, J. Lee, Versatile strategy for tuning orr activity of a single fe-n4 site by controlling electron-withdrawing/donating properties of a carbon plane. J. Am. Chem. Soc. **141**(15), 6254–6262 (2019). https://doi.org/10.1021/jacs.8b13543

37. G. Zhang, Y. Jia, C. Zhang, X. Xiong, K. Sun et al., A general route via formamide condensation to prepare atomically dispersed metal–nitrogen–carbon electrocatalysts for energy technologies. Energy Environ. Sci. **12**(4), 1317–1325 (2019). https://doi.org/10.1039/c9ee00162j

38. P. Yin, T. Yao, Y. Wu, L. Zheng, Y. Lin et al., Single cobalt atoms with precise n-coordination as superior oxygen reduction reaction catalysts. Angew. Chem. Int. Ed. **55**(36), 10800–10805 (2016). https://doi.org/10.1002/ange.201604802

39. H. Zhang, H.T. Chung, D.A. Cullen, S. Wagner, U.I. Kramm, K.L. More, P. Zelenay, G. Wu, High-performance fuel cell cathodes exclusively containing atomically dispersed iron active sites. Energy Environ. Sci. **12**, 2548–2558 (2019). https://doi.org/10.1039/c9ee00877b

40. Y. Deng, B. Chi, J. Li, G. Wang, L. Zheng et al., Atomic Fe-doped MOF-derived carbon polyhedrons with high active-center density and ultra-high performance toward pem fuel cells. Adv. Energy Mater. **9**(13), 1802856 (2019). https://doi.org/10.1002/aenm.201802856

41. Z. Yang, B. Chen, W. Chen, Y. Qu, F. Zhou et al., Directly transforming copper (i) oxide bulk into isolated single-atom copper sites catalyst through gas-transport approach. Nat. Commun. **10**(1), 3734 (2019). https://doi.org/10.1038/s41467-019-11796-4

42. G. Zhang, L. Wang, Y. Hao, X. Jin, Y. Xu, Y. Kuang, L. Dai, X. Sun, Unconventional carbon: alkaline dehalogenation of polymers yields n-doped carbon electrode for high-performance

capacitive energy storage. Adv. Funct. Mater. **26**(19), 3340–3348 (2016). https://doi.org/10.1002/adfm.201505533

43. E. Dervishi, Z. Ji, H. Htoon, M. Sykora, S.K. Doorn, Raman spectroscopy of bottom-up synthesized graphene quantum dots: size and structure dependence. Nanoscale **11**(35), 16571–16581 (2019). https://doi.org/10.1039/c9nr05345j

44. J. Xu, J. Zhu, X. Yang, S. Cao, J. Yu, M. Shalom, M. Antonietti, Synthesis of organized layered carbon by self-templating of dithiooxamide. Adv. Mater. **28**(31), 6727–6733 (2016). https://doi.org/10.1002/adma.201600707

45. H. Jin, H. Zhou, D. He, Z. Wang, Q. Wu, Q. Liang, S. Liu, S. Mu, MOF-derived 3d Fe-N-S co-doped carbon matrix/nanotube nanocomposites with advanced oxygen reduction activity and stability in both acidic and alkaline media. Appl. Catal. B **250**(5), 143–149 (2019). https://doi.org/10.1016/j.apcatb.2019.03.013

46. Y. Kuang, G. Feng, P. Li, Y. Bi, Y. Li, X. Sun, Single-crystalline ultrathin nickel nanosheets array from in situ topotactic reduction for active and stable electrocatalysis. Angew. Chem. Int. Ed. **55**(2), 693–697 (2016). https://doi.org/10.1002/ange.201509616

47. C. Pean, B. Daffos, B. Rotenberg, P. Levitz, M. Haefele, P.-L. Taberna, P. Simon, M. Salanne, Confinement, desolvation, and electrosorption effects on the diffusion of ions in nanoporous carbon electrodes. J. Am. Chem. Soc. **137**(39), 12627–12632 (2015). https://doi.org/10.1021/jacs.5b07416

48. Y. Chen, S. Ji, S. Zhao, W. Chen, J. Dong et al., Enhanced oxygen reduction with single-atomic-site iron catalysts for a zinc-air battery and hydrogen-air fuel cell. Nat. Commun. **9**(1), 1–12 (2018). https://doi.org/10.1038/s41467-018-07850-2

49. G. Zhang, H. Luo, H. Li, L. Wang, B. Han et al., ZnO-promoted dechlorination for hierarchically nanoporous carbon as superior oxygen reduction electrocatalyst. Nano Energy **26**, 241–247 (2016). https://doi.org/10.1016/j.nanoen.2016.05.029

50. C. Weidenthaler, A.-H. Lu, W. Schmidt, F. Schüth, X-ray photoelectron spectroscopic studies of pan-based ordered mesoporous carbons (OMC). Microporous Mesoporous Mater. **88**(1–3), 238–243 (2006). https://doi.org/10.1016/j.micromeso.2005.09.015

51. L. Zhang, Z. Xia, Mechanisms of oxygen reduction reaction on nitrogen-doped graphene for fuel cells. J. Phys. Chem. C **115**(22), 11170–11176 (2011). https://doi.org/10.1021/jp201991j

52. M. Wang, L. Árnadóttir, Z.J. Xu, Z. Feng, In situ X-ray absorption spectroscopy studies of nanoscale electrocatalysts. Nano-Micro Lett. **11**(1), 47 (2019). https://doi.org/10.1007/s40820-019-0277-x

53. Y. Chang, F. Hong, C. He, Q. Zhang, J. Liu, Nitrogen and sulfur dual-doped non-noble catalyst using fluidic acrylonitrile telomer as precursor for efficient oxygen reduction. Adv. Mater. **25**(34), 4794–4799 (2013). https://doi.org/10.1002/adma.201301002

54. I.-Y. Jeon, H.-J. Choi, S.-M. Jung, J.-M. Seo, M.-J. Kim, L. Dai, J.-B. Baek, Large-scale production of edge-selectively functionalized graphene nanoplatelets via ball milling and

their use as metal-free electrocatalysts for oxygen reduction reaction. J. Am. Chem. Soc. **135**(4), 1386–1393 (2012). https://doi.org/10.1021/ja3091643

55. Y. Chen, S. Ji, Y. Wang, J. Dong, W. Chen et al., Isolated single iron atoms anchored on n-doped porous carbon as an efficient electrocatalyst for the oxygen reduction reaction. Angew. Chem. Int. Ed. **56**(24), 6937–6941 (2017). https://doi.org/10.1002/ange.201703992

56. D. Geng, S. Yang, Y. Zhang, J. Yang, J. Liu et al., Nitrogen doping effects on the structure of graphene. Appl. Surf. Sci. **257**(21), 9193–9198 (2011). https://doi.org/10.1016/j.apsusc.2011.05.131

57. J. Shui, M. Wang, F. Du, L. Dai, N-doped carbon nanomaterials are durable catalysts for oxygen reduction reaction in acidic fuel cells. Sci. Adv. **1**(1), e1400129 (2015). https://doi.org/10.1126/sciadv.1400129

58. D. Gu, Y. Zhou, R. Ma, F. Wang, Q. Liu, J. Wang, Facile synthesis of N-doped graphene-like carbon nanoflakes as efficient and stable electrocatalysts for the oxygen reduction reaction. Nano-Micro Lett. **10**(2), 29 (2018). https://doi.org/10.1007/s40820-017-0181-1

59. M. Xiao, L. Gao, Y. Wang, X. Wang, J. Zhu et al., Engineering energy level of metal center: Ru single-atom site for efficient and durable oxygen reduction catalysis. J. Am. Chem. Soc. **141**(50), 19800–19806 (2019). https://doi.org/10.1021/jacs.9b09234

60. J. Liang, Y. Jiao, M. Jaroniec, S.Z. Qiao, Sulfur and nitrogen dual-doped mesoporous graphene electrocatalyst for oxygen reduction with synergistically enhanced performance. Angew. Chem. Int. Ed. **51**(46), 11496–11500 (2012). https://doi.org/10.1002/ange.201206720

61. Z. Jiang, W. Sun, H. Shang, W. Chen, T. Sun et al., Atomic interface effect of single atom copper catalyst for enhanced oxygen reduction reaction. Energy Environ. Sci. **12**, 3508–3514 (2019). https://doi.org/10.1039/c9ee02974e

62. A.K. Fajrial, M.F. Abdulkarim, A.G. Saputro, M.K. Agusta, H.K. Dipojono, Boron and nitrogen co-doping configuration on pyrolyzed Fe-N$_4$/C catalyst. Procedia Eng. **170**, 131–135 (2017). https://doi.org/10.1016/j.proeng.2017.03.028

63. R.A. Sidik, A.B. Anderson, N.P. Subramanian, S.P. Kumaraguru, B.N. Popov, O$_2$ reduction on graphite and nitrogen-doped graphite: experiment and theory. J. Phys. Chem. B **110**(4), 1787–1793 (2006). https://doi.org/10.1021/jp055150g

64. H. Jin, H. Zhou, W. Li, Z. Wang, J. Yang et al., In situ derived Fe/N/S-codoped carbon nanotubes from ZIF-8 crystals as efficient electrocatalysts for the oxygen reduction reaction and zinc–air batteries. J. Mater. Chem A **6**(41), 20093–20099 (2018). https://doi.org/10.1039/c8ta07849a

65. J. Meng, C. Niu, L. Xu, J. Li, X. Liu et al., General oriented formation of carbon nanotubes from metal–organic frameworks. J. Am. Chem. Soc. **139**(24), 8212–8221 (2017). https://doi.org/10.1021/jacs.7b01942

66. H. Xu, D. Cheng, D. Cao, X.C. Zeng, A universal principle for a rational design of single-atom electrocatalysts. Nat. Catal. **1**(5), 339 (2018). https://doi.org/10.1038/s41929-018-0063-z